RSC Advances

PAPER

Cite this: RSC Adv., 2018, 8, 28179

Fabrication of Ag_3PO_4/GO/$NiFe_2O_4$ composites with highly efficient and stable visible-light-driven photocatalytic degradation of rhodamine B

Tianhong Zhou,[ab] Guozhen Zhang,*[a] Hao Yang,[a] Hongwei Zhang,[a] Ruini Suo,[b] Yingshuang Xie[c] and Gang Liu[b]

Received 6th April 2018
Accepted 19th July 2018

DOI: 10.1039/c8ra02962h

rsc.li/rsc-advances

Effective visible-light-driven Ag_3PO_4/GO/$NiFe_2O_4$ *Z*-scheme magnetic composites were successfully fabricated by a simple ion-exchange deposition method. The Ag_3PO_4/GO/$NiFe_2O_4$ (8%) composite exhibited excellent photocatalytic activity (degradation efficiency was ~96% within 15 min and kinetic constant reached 0.1956 min^{-1}) and stability when compared to Ag_3PO_4, $NiFe_2O_4$, and Ag_3PO_4/$NiFe_2O_4$ for rhodamine B (RhB) degradation. Furthermore, by electrochemical and fluorescence measurements, the Ag_3PO_4/GO/$NiFe_2O_4$ (8%) material also showed larger transient photocurrent, lower impedance, and longer fluorescence lifetime (7.82 ns). Comparing the activity result dependence with characterization results, it was indicated that photocatalytic activity depended on fast charge transfer from Ag_3PO_4 to $NiFe_2O_4$ through GO sheet. The h^+ and $\cdot O_2^-$ species played important roles in RhB degradation under visible-light. A possible *Z*-scheme mechanism is proposed over the Ag_3PO_4/GO/$NiFe_2O_4$ (8%) composite. This study might provide a promising visible light responsive photocatalyst for the photocatalytic degradation of organic dyes in wastewater.

1. Introduction

Nowadays, abundant textile dyes have been discharged into the environment with the development of the economy and industry. This poses a serious threat to the environment and human health worldwide.[1–4] Developing environment-friendly, effective, stable and low-cost technology for water treatment is one of the key issues.[5] Among various dye wastewater treatment technologies (such as traditional biological methods, adsorption, reverse osmosis, coagulation, ozonation, electrochemical method, and Fenton process),[6–14] semiconductor-based photocatalysis allows the use of sunlight, which is a clean and renewable source of energy, for the destruction of dye pollutants.[15–18] To date, various metal oxides and sulfide and phosphate composites have been investigated for the development of effective photocatalysts.[19–21] Recently, significant attention has been directed toward the design and synthesis of highly efficient visible-light-driven photocatalysts (such as Ag_3PO_4 and AgBr) that can utilize solar energy.[22,23] However, Ag_3PO_4 suffers from poor photostability due to fast photoreduction to metallic Ag.[24–27] Therefore, it is urgently required to develop effective strategies to improve the stability of Ag_3PO_4 while simultaneously maintaining or enhancing its photocatalytic performance.[28,29]

Many efforts have been made to overcome the above-mentioned disadvantages, and a variety of Ag_3PO_4-based composite photocatalysts were suggested using methods, including hybridization, morphology control, and semiconductor hetero-coupling.[30] The development of multifunctional adsorption materials has been a major area of focus in the field of contaminant remediation over the last decade. Magnetic nanomaterials have attracted much attention because of their unique physical and chemical properties and potential applications in the separation and removal of pollutants from the environment.[31] Ferrites are one of the most promising photocatalysts with the characteristic behavior of absorbing visible light, and possess band gaps in the range 1.1–2.3 eV.[32] Moreover, ferrites overcome the technical problem of separation and reuse as they are magnetically separable.[33,34] Among the class of ferrites, nickel ferrite ($NiFe_2O_4$) is significant because of its excellent chemical stability, remarkable mechanical hardness, high electromagnetic performance and ferromagnetic behavior.[35] Some researchers found that ferrite semiconductors could inhibit Ag_3PO_4 photocorrosion, according to the previous reports.[27,36] However, the semiconductor–semiconductor contact interface is a crucial factor in ensuring continuous flow of electrons between the source and target photocatalysts.[37]

[a]School of Environmental and Municipal Engineering, Lanzhou Jiaotong University, Lanzhou 730000, P. R. China. E-mail: zhangguozhen@mail.lzjtu.cn

[b]Research & Development Center for Eco-material and Eco-chemistry, Lanzhou Institute of Chemical Physics, Chinese Academy of Sciences, Lanzhou 730000, P. R. China

[c]Gansu Import and Export Inspection and Quarantine Bureau Inspection and Quarantine Integrated Technology Center, Lanzhou 730000, P. R. China

Graphene-oxide (GO), similar to graphene, has attracted great attention because of its unique properties. Particularly, great efforts have been devoted towards the preparation of semiconductor/GO composites aimed at improving charge transportation and separation.[2,38] However, if the contact interfaces of Ag_3PO_4–$NiFe_2O_4$ composites could introduce a solid electron mediator (GO), whose effective suppression of charge recombination would result in the improvement of photocatalytic activity and stability.

Herein, visible-light-driven Ag_3PO_4/GO/$NiFe_2O_4$ composites were successfully fabricated by a simple ion-exchange deposition method and showed remarkably enhanced photocatalytic activity as compared to Ag_3PO_4, $NiFe_2O_4$, and Ag_3PO_4/$NiFe_2O_4$ for RhB degradation under visible light irradiation. Based on characterization results of all samples, it was indicated that the photocatalytic activity depended on efficient photogenerated charge separation. Moreover, Ag_3PO_4/GO/$NiFe_2O_4$ (8%) could be easily removed from water by adding an external magnetic field and could be reused. h^+ and $\cdot O_2^-$ species played important roles in RhB degradation under visible-light. A possible *Z*-scheme mechanism for RhB degradation over the Ag_3PO_4/GO/$NiFe_2O_4$ (8%) photocatalyst is proposed.

2. Experimental

2.1. Catalyst preparation

2.1.1 Synthesis of Ag_3PO_4. All reagents were of analytical grade and used without further purification. Ammonia solution (1 M) was slowly added to 100 mL (15.1 g) $AgNO_3$ solution dropwise under vigorous stirring to form silver ammonia solution. Subsequently, 100 mL Na_2HPO_4 (6.82 g) was added dropwise to the above dispersion with mechanical agitation, followed by sonication for another 20 min. Finally, the precipitates in the solution were centrifuged and meticulously washed with deionized water. The as-obtained samples were dried at 65 °C for 12 h under vacuum.

2.1.2 Synthesis of $NiFe_2O_4$. $NiFe_2O_4$ nanostructure was successfully prepared by a simple hydrothermal process according to the previous literature.[39] Briefly, to an aqueous solution (200 mL) containing $Ni(NO_3)_2 \cdot 6H_2O$ (2.27 g) and $Fe(NO_3)_3 \cdot 9H_2O$ (5.34 g), NaOH solution (2.0 M) was added with magnetic stirring at room temperature (RT). The mixture was then transferred to a Teflon-lined stainless-steel autoclave of 140 mL capacity. The sealed tank was heated to and maintained at 180 °C for 12 h in an oven and cooled to RT. The resultant brown precipitates were collected by filtration and washed with water and ethanol more than 3 times, and finally dried in an oven at 60 °C for 12 h.

2.1.3 Synthesis of graphite oxide (GO). GO was prepared from natural flake graphite according to the modified Hummer's method.[40] In a typical synthesis, 2.0 g graphite powder was added to 80 mL cold (0 °C) concentrated H_2SO_4 in an ice bath. Then, $NaNO_3$ (4.0 g) and $KMnO_4$ (8.0 g) were added gradually under stirring and the temperature of the mixture was maintained below 10 °C. The reaction mixture was continually stirred for 4 h at temperature below 10 °C. Successively, the mixture was stirred at 35 °C for 4 h, and then diluted with 200 mL deionized (DI) water. After adding DI water, the mixture was stirred for 1 h. The reaction was then terminated by adding 15 mL 30% H_2O_2 solution. The solid product was separated by centrifugation and washed repeatedly with 5% HCl solution until sulfate could not be detected with $BaCl_2$. For further purification, the resultant solid was re-dispersed in DI water and dialyzed for 3 days to remove residual salts and acids. The suspension was dried in a vacuum oven at 45 °C for 48 h to obtain graphite oxide.

2.1.4 Synthesis of Ag_3PO_4/$NiFe_2O_4$. Ag_3PO_4/$NiFe_2O_4$ composite was prepared by a simple ion-exchange deposition method. The loading of $NiFe_2O_4$ was 8% for Ag_3PO_4/$NiFe_2O_4$ composite. Typically, 1 M ammonia solution was slowly added to 100 mL (15.1 g) $AgNO_3$ solution dropwise with vigorous stirring to form silver ammonia solution. Then, a certain amount of $NiFe_2O_4$ sample was added under vigorous stirring and sonication for 30 min. Na_2HPO_4 (6.82 g, 100 mL) was added dropwise to the above dispersion with mechanical agitation, followed by sonication for another 20 min. Finally, the obtained precipitates were centrifuged and washed with deionized water. The as-obtained samples were dried at 65 °C for 12 h under vacuum.

2.1.5 Synthesis of GO/$NiFe_2O_4$. GO/$NiFe_2O_4$ was prepared by a hydrothermal process as previously reported.[41] A certain amount of GO (138 mL, 5 mg mL^{-1}) solution dissolved in 62 mL deionized water. Next, 2.27 g $Ni(NO_3)_2 \cdot 6H_2O$ and 5.34 g $Fe(NO_3)_3 \cdot 9H_2O$ were added with stirring at room temperature for a certain period of time. Then, excess NaOH was added to the solution slowly until pH = 10.5. The mixture was transferred to a Teflon-lined autoclave and maintained at 180 °C for 12 h. The composites were washed with deionized water several times and dried at 60 °C for 12 h under vacuum. The theoretical loading of GO was 30% in GO/$NiFe_2O_4$ catalyst.

2.1.6 Synthesis of Ag_3PO_4/GO/$NiFe_2O_4$ composites. The as-obtained GO/$NiFe_2O_4$ powder was used for composite preparation. The synthesis of Ag_3PO_4/GO/$NiFe_2O_4$ composites was carried out by a simple ion-exchange deposition method.[41] The GO/$NiFe_2O_4$ loading was x% ($x = 4$, 8, 12 and 16) and denoted as Ag_3PO_4/GO/$NiFe_2O_4$(x%). Typically, taking Ag_3PO_4/GO/$NiFe_2O_4$ (8%) catalyst as an example, 1 M ammonia solution was slowly added to 100 mL (15.1 g) $AgNO_3$ solution dropwise under vigorous stirring to form silver ammonia solution. Subsequently, 0.64 g GO/$NiFe_2O_4$ (30%) sample was added under vigorous stirring and sonicated for 30 min. Then, 100 mL Na_2HPO_4 (6.82 g) was added dropwise to the above dispersion with mechanical agitation and then sonicated for another 20 min. The obtained precipitate was centrifuged, washed with deionized water several times, and dried at 65 °C for 12 h. Finally, the products were collected and ground to powder by an agate mortar for further use.

2.2. Characterization techniques

The phase formation in the composites was investigated *via* powder X-ray diffraction (XRD) on a Rigaku D/max 2400/PC diffractometer with Cu K_α ($\lambda = 1.5406$ Å) at 40 kV and 150 mA. Diffraction patterns in the 5–90° region were recorded at the rate of 5° min^{-1}. The chemical compositions and chemical bonding states of the specimens were defined by X-ray photoelectron spectroscopy (XPS, equipped with a standard monochromatic Al K$_\alpha$ source ($h\nu$) 1486.6 eV, ESCALAB 250Xi, ThermoFisher Scientific, UK). Field emission scanning electron microscopy (FE-SEM, HITACHI S-4800) and energy-dispersive X-ray spectroscopy analysis (Thermo Fisher, Noran 7) were employed for detailed discussion of morphologies of the specimens. Transmission electron microscopy (TEM) and HRTEM images were taken with a Tecnai-G2-F30 field emission transmission electron microscope operating at an accelerating voltage of 300 kV. Absorbance spectra of the samples were recorded on a UV-vis spectrometer (UV-765 UV-vis spectrometer, Shanghai Jingke) in the range of 200–800 nm. UV-vis diffuse reflectance spectra (DRS) of the samples were recorded using a UV/Vis/NIR PerkinElmer Lambda 950 double beam spectrophotometer equipped with a standard 150 mm integrating sphere, and total reflectance was measured relative to a $BaSO_4$ reference. TOC was determined using a TOC analyzer (Elementar vario TOC cube, Hanau, Germany). Magnetic hysteresis loops at room temperature were obtained using a VSM (LAKESHORE-7304, USA) at room temperature. The photoluminescence (PL) spectra of samples were investigated on an Edinburgh FL/FS900 spectrophotometer with excitation wavelength of 350 nm.

2.3. Photocatalytic activities measurement

Photocatalytic activities of all the samples were measured by photocatalytic degradation of aqueous RhB (10 mg L^{-1}) solutions, where the photocatalytic reaction was conducted in a specially designed glass reactor equipped with a water-cooling system to maintain the solution at room temperature. The light source was designed for 300 W xenon short arc lamps equipped with ultraviolet cutoff filter (providing visible light ≥400 nm). Typically, 20 mg sample was added to 100 mL aqueous solution of organic dye, and the reactant was mixed quickly. Prior to irradiation, the suspension was magnetically stirred in the dark for 20 min to establish adsorption–desorption equilibrium between photocatalysts and organic dyes. The as-obtained solution was then exposed to irradiation with fixed distance of 15 cm under magnetic stirring. At regular intervals of time, 4 mL of the suspension was withdrawn and immediately filtered with a filter membrane to remove the photocatalysts; the initial concentration of RhB (10 mg L^{-1}) in the solution was defined as C_0 and the resulting concentration of the solution was named C. The absorbance of the filtered solution was measured using a UV visible spectrophotometer. The C/C_0 ratio as a function of irradiation time was used to evaluate the degradation efficiency of photocatalyst. In addition, to accomplish the next cycle of experiment, the catalyst was recovered from the solution using an external magnet after completion of the reaction. The magnetically recovered-catalyst was washed, dried, and weighed for further use.

2.4. Electrochemical measurements

All electrochemical measurements were recorded on an electrochemical analyzer (CHI660E) in a homemade standard three-electrode quartz cell comprising an organic glass enclosure with a quartz window and a 1.2 cm diameter opening opposite the window to the clamped working electrode. A platinum plate was used as the counter electrode and a saturated calomel electrode (SCE) was used as the reference electrode. The working electrode was prepared by drop-coating sample suspensions and Nafion directly on a pre-cleaned indium tin oxide glass (ITO glass) surface. The surface area of the working electrode exposed to the electrolyte was about 0.95 cm^2. The electrolyte was 0.01 M Na_2SO_4 aqueous solution without any additives. The visible light irradiation source was a 300 W Xe lamp system equipped with 400 nm cut-off filter.

3. Results and discussion

3.1. X-ray diffraction analysis

The crystallographic structure and phase purity of all samples were examined by powder X-ray diffraction. As shown in Fig. 1, all the diffraction peaks of $NiFe_2O_4$ resemble the cubic spinel structure (JCPDS no. 10-0325). The diffraction peaks at 18.39, 30.29°, 35.70°, and 62.92° were indexed to the (111), (220), (311) and (440) crystal planes of $NiFe_2O_4$, respectively.[42] In the spectrum of Ag_3PO_4, all of the peaks could be indexed to the cubic structural phase (JCPDS no. 06-0505).[43,44] The peaks at 10.6° were attributed to the (002) crystal planes of GO (marked with ◆).[45] In the case of Ag_3PO_4/GO/$NiFe_2O_4$ (8%) nanocomposite, the major diffraction peaks (marked with ♥ and ♣) could be clearly indexed to the cubic Ag_3PO_4 phase and cubic $NiFe_2O_4$ spinel phase. This result further illustrates that the Ag_3PO_4/GO/$NiFe_2O_4$ composite was successfully synthesized by a simple ion-exchange deposition method.

3.2. X-ray photoelectron spectroscopy analysis

XPS analysis was performed to investigate the chemical composition and bonding state of the Ag_3PO_4/GO/$NiFe_2O_4$ (8%) photocatalyst. Fig. 2a shows the XPS survey (wide-scan) spectrum confirming the existence of P, C, Ag, O, Fe, and Ni in the Ag_3PO_4/GO/$NiFe_2O_4$ (8%) composite. In Fig. 2b, Ag 3d XPS spectrum shows that peaks located at 374.03 and 367.96 eV can be ascribed to Ag 3d$_{3/2}$ and Ag 3d$_{5/2}$, respectively, indicating the existence of Ag^+.[46,47] No peaks were found at 369.2 or 375.8 eV,

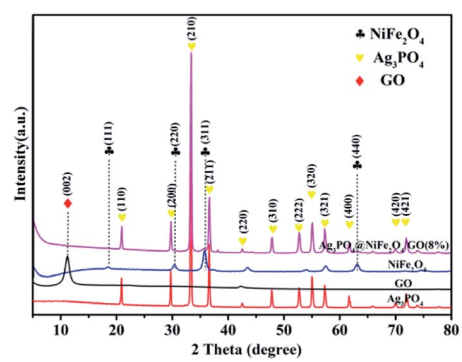

Fig. 1 XRD patterns of Ag_3PO_4, GO, $NiFe_2O_4$, and Ag_3PO_4/GO/$NiFe_2O_4$ (8%) samples.

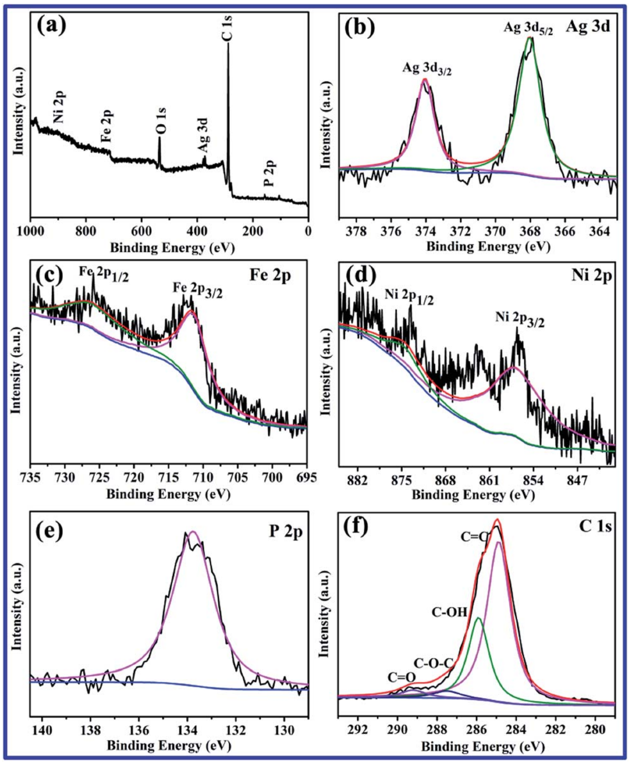

Fig. 2 XPS spectra of $Ag_3PO_4/GO/NiFe_2O_4$ (8%) sample. (a) The fully scanned spectrum, and high resolution spectra of (b) Ag 3d, (c) Fe 2p, (d) Ni 2p, (e) P 2p, and (f) C 1s.

verifying the absence of Ag^0.[48] As shown in Fig. 2c, the peaks centered at 711.3 eV (Fe $2p_{3/2}$) and 725.6 eV (Fe $2p_{1/2}$) might be ascribed to Fe^{3+}.[49] XPS peaks of Ni 2p can be found at 856.7 eV and 874.4 eV (Fig. 2d) and can be assigned to Ni $2p_{3/2}$ and Ni $2p_{1/2}$, respectively, corresponding to Ni^{2+}.[50] The observed P 2p binding energies at 133.8 eV were typical of oxidized phosphate species (PO_4^{3-}) in Ag_3PO_4 (shown in Fig. 2e).[51,52] The high resolution spectrum for the C 1s region revealed four carbon peaks, which were located at 284.9 eV, 286.3 eV, 287.5 eV, and 289.3 eV (see Fig. 2f). The peaks at 284.9 and 286.3 eV are typical of C=C and C–OH bonds, and the peaks at 287.5 and 289.3 eV are usually associated with C–O–C and C=O bonds, respectively. These results are in good agreement with those previously reported.[1,53] The abovementioned XPS results confirmed the coexistence of $GO/NiFe_2O_4$ and Ag_3PO_4 in $Ag_3PO_4/GO/NiFe_2O_4$ composites.

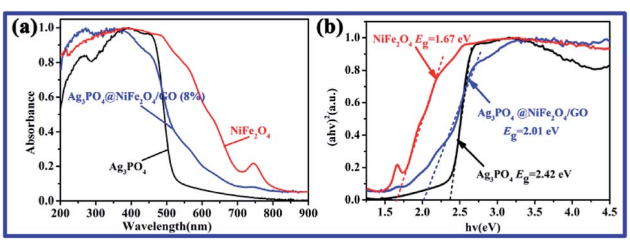

Fig. 3 (a) UV-vis DRS and (b) the plot of $(\alpha h\nu)^2$ *vs.* $h\nu$ of $NiFe_2O_4$, Ag_3PO_4, and $Ag_3PO_4/GO/NiFe_2O_4$ (8%).

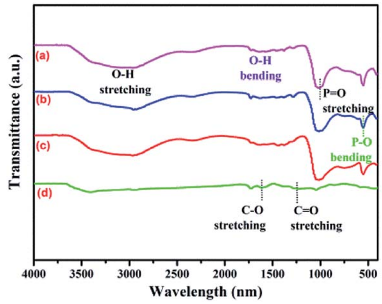

Fig. 4 FTIR spectra of (a) $Ag_3PO_4/GO/NiFe_2O_4$ (8%), (b) $Ag_3PO_4/NiFe_2O_4$, (c) Ag_3PO_4 and (d) GO samples.

3.3. UV-vis DRS FTIR transmittance spectroscopy analysis

Fig. 3a presents the UV-vis diffuse reflectance spectra (DRS) of $NiFe_2O_4$, Ag_3PO_4, and $Ag_3PO_4/GO/NiFe_2O_4$ (8%) samples, which are widely used to measure the optical properties of semiconductor materials. Clearly, the $Ag_3PO_4/GO/NiFe_2O_4$ (8%) composite absorbed in both ultraviolet light and visible light regions and the largest wavelength of incident light was about 490 nm. The estimated values of band gap energies (E_g) were obtained by extrapolation of the linear parts of the curves obtained by plotting $(\alpha h\nu)^2$ *versus* $h\nu$. As shown in Fig. 3b, E_g of Ag_3PO_4, $NiFe_2O_4$, and $Ag_3PO_4/GO/NiFe_2O_4$ (8%) were 2.42 eV 1.67 eV, and 2.01 eV, respectively. These values are in agreement with those obtained in earlier reports.[54,55] Fig. 4 shows the FTIR spectra of GO, Ag_3PO_4, $Ag_3PO_4//NiFe_2O_4$, and $Ag_3PO_4/GO/NiFe_2O_4$ (8%) samples over the range of 400–4000 cm^{-1}. The strong bands centered at 555 cm^{-1} were assigned to the O=P–O bending vibration and those at 1010 cm^{-1} were assigned to the asymmetric stretching of PO_4^{3-} groups.[56] The 1650 cm^{-1} band was ascribed to the H_2O bending mode. The absorption band at 3400–3650 cm^{-1} was related to the stretching vibration of adsorbed water.[57,58] As expected for $NiFe_2O_4$ structures, there were two broad bands with low transmittances in the range of 400–525 cm^{-1} and 560–630 cm^{-1} that were observed in each spectrum.[59–61] Accordingly, these two absorption bands were related to tetrahedral and octahedral vibrational trivalent cations of Fe^{3+}. Different vibrational modes in the octahedral and tetrahedral components were attributed to linked distance

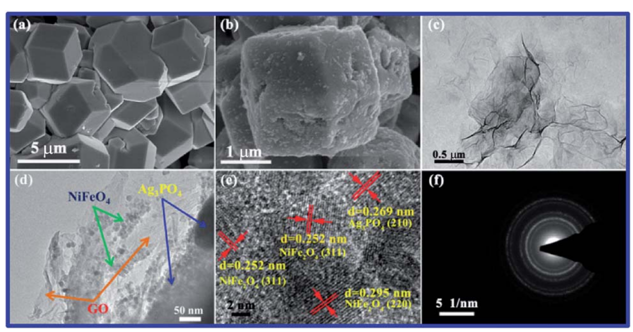

Fig. 5 SEM images of Ag_3PO_4 (a) and $Ag_3PO_4/NiFe_2O_4$ (b); TEM images of GO (c) and $Ag_3PO_4/GO/NiFe_2O_4$ (8%) (d); HRTEM (e) and SAED (f) of $Ag_3PO_4/GO/NiFe_2O_4$ (8%) composite.

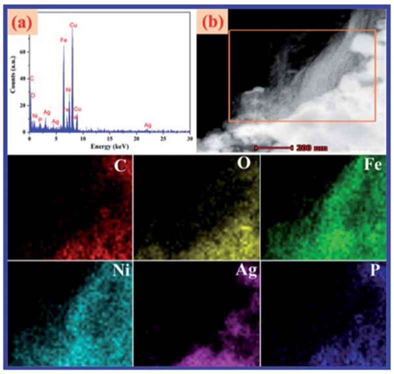

Fig. 6 (a) EDX and (b) HAADF-STEM and elemental mapping images of $Ag_3PO_4/GO/NiFe_2O_4$ (8%) composite.

differences of $Fe^{3+}–O^{2-}$ in the two modes.[59] In the spectrum of GO, the absorption bands at 1620 cm^{-1} and 1400 cm^{-1} corresponded to the C–O stretching and deformation vibration from carboxyl, and the absorption bands centered at 3390 cm^{-1} and 1247 cm^{-1} were attributed to the O–H stretching and CO stretching vibrations of the –COOH group.[62]

3.4. FE-SEM and TEM analysis

To better understand the structures and morphologies of GO, Ag_3PO_4, and $Ag_3PO_4/GO/NiFe_2O_4$ (8%), characterization of FE-SEM and TEM images of all the samples was performed. As shown in Fig. 5a, pure Ag_3PO_4 has cubic structure with average diameter of 4 μm. $NiFe_2O_4$ particles were dispersed on Ag_3PO_4 surface and the average particle diameter was 50 nm (see Fig. 5b). TEM images of GO and $Ag_3PO_4/GO/NiFe_2O_4$ (8%) samples are given in Fig. 5c and d, respectively. Clearly, $Ag_3PO_4/GO/NiFe_2O_4$ (8%) has a large number of $NiFe_2O_4$ nanoparticles and the GO sheet was located on the Ag_3PO_4 surface. *d*-spacing fringes of 0.269 nm matching (210) planes of cubic Ag_3PO_4 phase and *d*-spacing fringes of 0.295 and 0.252 nm matching the (220) and (311) planes of cubic $NiFe_2O_4$ spinel structure are also observed in Fig. 5e. SAED of $Ag_3PO_4/GO/NiFe_2O_4$ (8%) exhibits an alternate lattice spacing characteristic (see Fig. 5f). All the above results indicate that $GO/NiFe_2O_4$ nanoparticles combined successfully with the Ag_3PO_4 surface. The energy dispersive X-ray (EDX) data proved the presence of Ag, P, O, Ni, Fe, and C in $Ag_3PO_4/GO/NiFe_2O_4$ (8%) (see Fig. 6a). In addition, Fig. 6b shows a dark field image of high-angle annular scanning transmission electron microscopy (HAADF-STEM). Moreover, elemental mapping of $Ag_3PO_4/GO/NiFe_2O_4$ (8%) samples distinctly indicated that the distributions of Ag, P, O, Ni, Fe, and C were relatively homogeneous on the $Ag_3PO_4/GO/NiFe_2O_4$ (8%) surface.

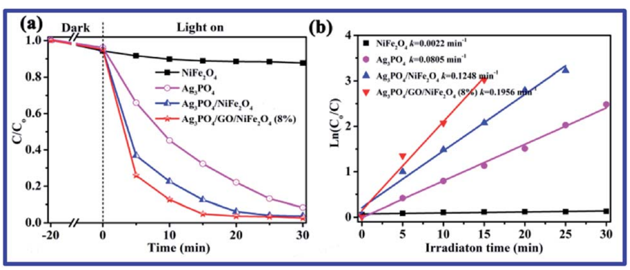

Fig. 7 (a) Photocatalytic activities of Ag_3PO_4, $NiFe_2O_4$, $Ag_3PO_4/NiFe_2O_4$, and $Ag_3PO_4/GO/NiFe_2O_4$ (8%) composites for RhB degradation, and (b) plots of $\ln(C_0/C)$ *versus* irradiation time.

3.5. Photocatalytic activity

As shown in Fig. 7a, $Ag_3PO_4/GO/NiFe_2O_4$ (8%) decomposed ~96% of RhB within 15 min of irradiation. More importantly, the photocatalytic activity of $Ag_3PO_4/GO/NiFe_2O_4$ (8%) exceeded that of other samples under the same conditions. The reaction rate constants (k, min^{-1}) were determined from the first-order equation: $\ln(C_0/C) = kt$. As shown in Fig. 7b, $Ag_3PO_4/GO/NiFe_2O_4$ (8%) exhibits higher rate constant ($k = 0.1956\ min^{-1}$) than those of Ag_3PO_4, $NiFe_2O_4$, and $Ag_3PO_4/NiFe_2O_4$.

To further demonstrate the excellent performance of $Ag_3PO_4/GO/NiFe_2O_4$ (8%) and other Ag_3PO_4-based photocatalysts, a detailed comparison of RhB degradation rate constant on Ag_3PO_4-based photocatalyst under visible light irradiation is shown in Table 1. The $Ag_3PO_4/GO/NiFe_2O_4$ (8%) photocatalyst exhibited excellent photocatalytic activity ($k = 0.1956\ min^{-1}$), further confirming its outstanding photocatalytic behavior.

In addition, the effect of different loadings of $GO/NiFe_2O_4$ over $Ag_3PO_4/GO/NiFe_2O_4$ on the photocatalytic activity was studied, as shown in Fig. 8a. Clearly, $Ag_3PO_4/GO/NiFe_2O_4$ (8%) showed excellent photocatalytic activity for RhB degradation. The UV-vis absorbance spectra of RhB solution with $Ag_3PO_4/GO/NiFe_2O_4$ (8%) under visible light irradiation at different times

Table 1 Photocatalytic degradation of RhB by Ag_3PO_4-based photocatalysts in aqueous solution

Photoactive nanocomposite	Initial dye conc. (mg L^{-1})	Catalyst dose (g L^{-1})	Rate constant (min^{-1})	Reference
$Ag_3PO_4/GO/NiFe_2O_4$ (8%)	10	0.2	0.1956	In this work
Ag_3PO_4	10	0.5	0.0372	63
$Ag_3PO_4/SnSe_2$	10	0.66	0.0724	64
Ag_3PO_4/RGO/Ag	10	0.5	0.1411	65
Ag_3PO_4/TiO_2	10	0.25	0.1300	66
TiO_2/Ag_3PO_4/GO	10	0.5	0.1281	67
$Ag_3PO_4/g\text{-}C_3N_4$	10	0.5	0.0739	68
$GO/Ag_3PO_4/g\text{-}C_3N_4$	10	0.4	0.162	69

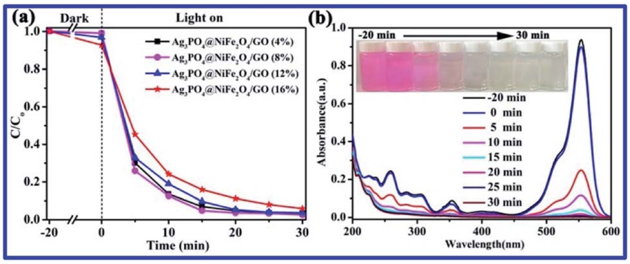

Fig. 8 (a) Photocatalytic activities of Ag_3PO_4/GO/$NiFe_2O_4$ (x%, x = 4, 8, 12, 16) for RhB degradation, (b) RhB solution UV-visible spectra at different irradiation times for Ag_3PO_4/GO/$NiFe_2O_4$ (8%).

are shown in Fig. 8b. It could be observed that the characteristic absorption peak at 553 nm steadily decreased as the exposure time increased during the process of RhB photodegradation. Correspondingly, the original color of RhB dye solution completely disappeared. This further indicated that Ag_3PO_4/GO/$NiFe_2O_4$ (8%) exhibited excellent photocatalytic activity for RhB decomposition under visible light.

As shown in Fig. 9a, the TOC result suggests that 43% of RhB was mineralized in the photocatalytic system of Ag_3PO_4/GO/$NiFe_2O_4$ (8%) composite within 30 min of irradiation. To investigate the magnetic properties of all samples, the M − H loop is depicted in Fig. 9b. M_s of pure $NiFe_2O_4$ and Ag_3PO_4/GO/$NiFe_2O_4$ (8%) composite were 34.56 and 2.92 emu g^{-1}, respectively. The Ag_3PO_4/GO/$NiFe_2O_4$ (8%) composite has good magnetic properties due to introduction of magnetic $NiFe_2O_4$. The Ag_3PO_4/GO/$NiFe_2O_4$ (8%) composite not only showed high

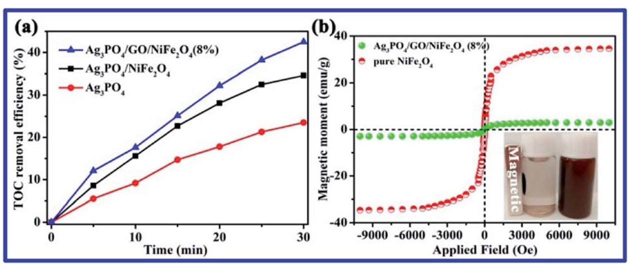

Fig. 9 (a) TOC removal efficiency for the photodegradation of RhB over pure Ag_3PO_4, Ag_3PO_4/$NiFe_2O_4$, and Ag_3PO_4/GO/$NiFe_2O_4$ (8%); (b) the M − H loops of $NiFe_2O_4$ and Ag_3PO_4/GO/$NiFe_2O_4$ (8%).

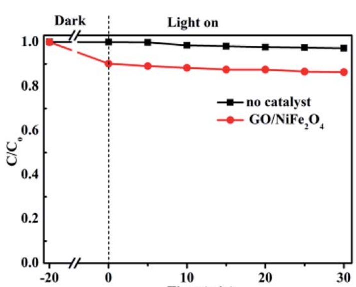

Fig. 10 Photocatalytic degradations of RhB in GO/$NiFe_2O_4$ and blank (no catalyst) systems with visible light irradiation.

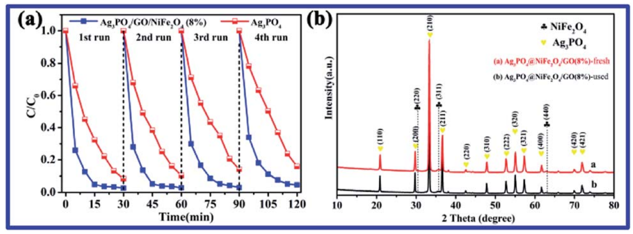

Fig. 11 (a) Stability tests of the Ag_3PO_4 and Ag_3PO_4/GO/$NiFe_2O_4$ (8%) composites. (b) XRD of Ag_3PO_4/GO/$NiFe_2O_4$ (8%) fresh and used samples.

photocatalytic activity for degradation of RhB, but also could be easily separated from water bodies, effectively avoiding secondary pollution. Apart from photocatalytic activity, the stability of the photocatalyst is also an important factor for practical application of this material.

Furthermore, control experiments were performed and the results were given in Fig. 10. Clearly, the RhB degradation efficiency was 2.9% without any photocatalyst under visible light after 30 min irradiation; this degradation was mainly due to the RhB self-sensitization effect.[10,70] The degradation efficiency of the GO/$NiFe_2O_4$ sample was lower (about 13.7%). Compared to the other samples, the GO/$NiFe_2O_4$ sample exhibited low photocatalytic activity for RhB degradation under visible light irradiation. These results further confirmed that the photocatalytic activity enhancement of Ag_3PO_4/GO/$NiFe_2O_4$ (8%) catalyst was not induced by the self-sensitization effect but rather by Ag_3PO_4.

3.6. Stability test of Ag_3PO_4/GO/$NiFe_2O_4$ (8%) sample

To study the photocatalytic stability of the Ag_3PO_4/GO/$NiFe_2O_4$ (8%) sample, cycling degradation experiments of RhB dyes were performed, and the results are shown in Fig. 11a. Clearly, Ag_3PO_4/GO/$NiFe_2O_4$ (8%) exhibited excellent stability during four cycles of degradation of RhB solution under visible-light irradiation. As shown in Fig. 11b, it was found that the used Ag_3PO_4/GO/$NiFe_2O_4$ (8%) catalyst had no significant difference between fresh sample and used sample in terms of crystal phase structure.

In addition, the Ag_3PO_4/GO/$NiFe_2O_4$ (8%) fresh and used catalysts were characterized by SEM (see Fig. 12). For Ag_3PO_4/GO/$NiFe_2O_4$ (8%)-fresh sample, the SEM result showed cubic structure morphology with size of ∼3 μm (see Fig. 12a).

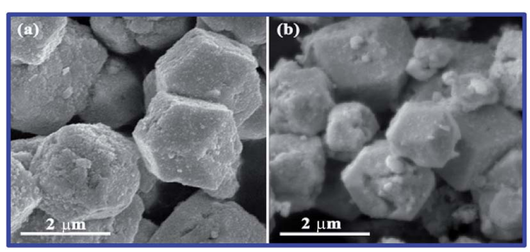

Fig. 12 SEM images of (a) Ag_3PO_4/GO/$NiFe_2O_4$ (8%)-fresh and (b) used samples for RhB degradation.

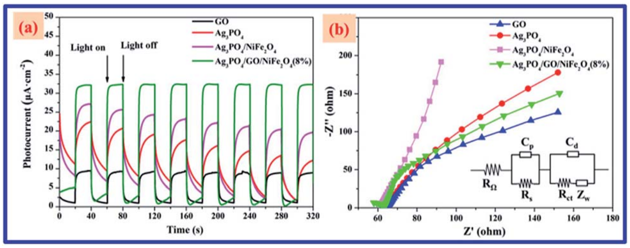

Fig. 13 (a) Transient photocurrent response and (b) electrochemical impedance spectroscopy (EIS) Nyquist plots of GO, Ag_3PO_4, $Ag_3PO_4/NiFe_2O_4$, and $Ag_3PO_4/GO/NiFe_2O_4$ (8%) electrodes in 0.01 M Na_2SO_4 aqueous solution.

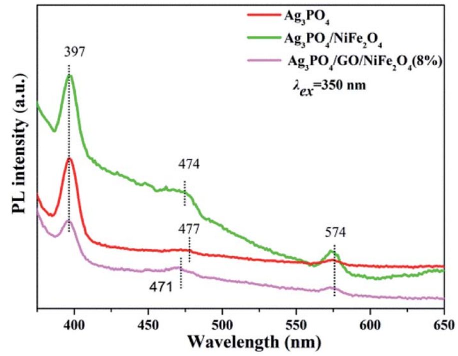

Fig. 14 Photoluminescence spectra of Ag_3PO_4, $Ag_3PO_4/NiFe_2O_4$ and $Ag_3PO_4/GO/NiFe_2O_4$ (8%) samples in pure water at excitation wavelength of 350 nm. [Catalyst] = 1 mg mL^{-1}.

Compared with the morphology of $Ag_3PO_4/GO/NiFe_2O_4$ (8%)-fresh sample, the morphology of the used photocatalyst showed slight photocorrosion phenomenon (shown in Fig. 12b). Recently, it was found that the introduction of other components (such as GO, g-C_3N_4, $ZnFe_2O_4$, PANI) on the surface of Ag_3PO_4 suppressed Ag_3PO_4 photocorrosion.[10,12,53,71] This result further implied that the presence of $GO/NiFe_2O_4$ enhanced the stability of Ag_3PO_4, which might be attributed to the protective role of $GO/NiFe_2O_4$ in the process of photocorrosion of Ag_3PO_4. Therefore, the $Ag_3PO_4/GO/NiFe_2O_4$ (8%) composite is a stable visible-light-driven photocatalyst for RhB degradation.

3.7. Electrochemical analysis

To further explore the role of GO in $Ag_3PO_4/GO/NiFe_2O_4$ (8%), electrochemical analyses, including transient photocurrent response and electrochemical impedance spectroscopy (EIS) Nyquist plots (shown in Fig. 13), of all samples were carried out. The transient photocurrent–time curves of pure GO, Ag_3PO_4, $Ag_3PO_4/NiFe_2O_4$, and $Ag_3PO_4/GO/NiFe_2O_4$ (8%) samples were measured by several on–off runs (see Fig. 13a). It was easily observed that the photocurrent over $Ag_3PO_4/GO/NiFe_2O_4$ (8%) electrode was greatly improved compared to that of the other electrodes. These results indicated that the $Ag_3PO_4/GO/NiFe_2O_4$ (8%) composite significantly enhanced photoelectric response compared with GO, Ag_3PO_4, and $Ag_3PO_4/NiFe_2O_4$ systems, which was beneficial for the former's enhanced photocatalytic activity.[72,73] In addition, Fig. 13b displays that the Nyquist plots from the EIS analysis cycled in 0.01 M Ns_2SO_4 electrolyte solution exhibit semicircles at high frequencies. Considering that the preparation of electrodes and the electrolyte used are identical, the high frequency semicircle is relevant to the resistance of the electrode.[74] In electrochemical spectra, the high-frequency arc corresponds to the charge transfer limiting process and can be attributed to double-layer capacitance (C_{dl}) in parallel with charge transfer resistance (R_{ct}) at the contact interface between the electrode and electrolyte solution.[75,76] In the Nyquist plots, the $Ag_3PO_4/GO/NiFe_2O_4$ (8%) sample exhibited the smallest semicircle compared with that of GO, Ag_3PO_4, and $Ag_3PO_4/NiFe_2O_4$ electrodes. The charge transfer resistance R_{ct} of $Ag_3PO_4/GO/NiFe_2O_4$ (8%) was 118.2 Ω, which was much smaller than that of Ag_3PO_4 and $Ag_3PO_4/NiFe_2O$. Clearly, the introduction of GO led to a significantly decreased diameter in the semicircular Nyquist plot as compared to that of $Ag_3PO_4/NiFe_2O_4$, suggesting faster charge transfer rate in the *Z*-scheme system.[77–79]

3.8. Photoluminescence intensity and lifetime analysis

Furthermore, the photoluminescence (PL) spectra of Ag_3PO_4, $Ag_3PO_4/NiFe_2O_4$, and $Ag_3PO_4/GO/NiFe_2O_4$ (8%) samples are displayed in Fig. 14. PL spectra of all samples were excited using excitation wavelength at 350 nm. Apparently, the fluorescence intensity of $Ag_3PO_4/GO/NiFe_2O_4$ (8%) decreased compared to that of Ag_3PO_4 and $Ag_3PO_4/NiFe_2O_4$ samples, further demonstrating that the fluorescence of $Ag_3PO_4/GO/NiFe_2O_4$ (8%) was quenched by the introduction of GO mediator. Generally, lower PL signal signifies higher separation efficiency of electron–hole pairs.[80] In other words, the PL results demonstrated the improved electron–hole pair separation efficiency of the $Ag_3PO_4/GO/NiFe_2O_4$ (8%) composite.

Table 2 Average fluorescence lifetimes of Ag_3PO_4, $Ag_3PO_4/NiFe_2O_4$ and $Ag_3PO_4/GO/NiFe_2O_4$ (8%) samples in pure H_2O; [catalyst] = 1 mg mL^{-1}

Samples	Lifetime, τ (ns)	Pre-exponential factors B	Average lifetime, $\langle\tau\rangle$ (ns)	χ^2
Ag_3PO_4	$\tau_1 = 9.53$	$B_1 = 33.36$	6.98	1.103
	$\tau_2 = 3.52$	$B_2 = 66.64$		
$Ag_3PO_4/NiFe_2O_4$	$\tau_1 = 4.38$	$B_1 = 27.01$	5.81	1.203
	$\tau_2 = 6.18$	$B_2 = 72.99$		
$Ag_3PO_4/GO/NiFe_2O_4$ (8%)	$\tau_1 = 8.40$	$B_1 = 51.14$	7.82	1.109
	$\tau_2 = 7.09$	$B_2 = 48.86$		

Fluorescence lifetimes were acquired by fitting the decay profiles with two exponential terms (see Table 2). Apparently, the average lifetimes of Ag_3PO_4, $Ag_3PO_4/NiFe_2O_4$, and $Ag_3PO_4/GO/NiFe_2O_4$ (8%) were 6.98, 5.81, and 7.82 ns, respectively. The slower PL decay kinetics and longer fluorescence lifetimes of $Ag_3PO_4/GO/NiFe_2O_4$ (8%) implied the photo-excited electron transfer from the conduction band (CB) of Ag_3PO_4 to the valence band (VB) of $NiFe_2O_4$ by GO mediator. The PL result is in good agreement with the electrochemical results.

3.9. Possible photocatalytic mechanism

Generally, $\cdot O_2^-$, h^+ and $\cdot OH$ play important roles in organic dye degradation.[81] To realize the underlying photocatalytic mechanism, various scavengers (1 mM EDTA-Na_2 for h^+, 1 mM isopropanol for $\cdot OH$, and 1 mM ascorbic acid for $\cdot O_2^-$) were added to the photocatalytic system.[79] As shown in Fig. 15, it is found that the degradation rate was drastically inhibited by addition of h^+ and $\cdot O_2^-$ capture agents EDTA-Na_2 and ascorbic acid, respectively, which further illuminated that h^+ and $\cdot O_2^-$ played important roles in RhB degradation process.

A possible mechanism is proposed for RhB degradation over $Ag_3PO_4/GO/NiFe_2O_4$ (8%) under visible-light irradiation (see Scheme 1). The *Z*-scheme mechanism reveals that the photocatalysts retain stronger oxidation and reduction ability, which deeply contribute to the improvement in photocatalytic activity.[82] The photogenerated electrons from $NiFe_2O_4$ can reduce O_2 to $\cdot O_2^-$ ($\varphi°(O_2/\cdot O_2^-) = -0.33$ V *vs.* NHE) through a one-electron reduction reaction.[83] This was mainly because the CB potential of $NiFe_2O_4$ was -0.60 eV. $\cdot O_2^-$ and h^+ species with strong oxidation abilities can degrade the RhB dye to organic intermediate products,[84] which was confirmed *via* TOC removal efficiency spectra of RhB eliminated by $Ag_3PO_4/GO/NiFe_2O_4$ (8%) composite (see Fig. 8a). This result further suggested that GO improved charge transportation and separation and enhanced photocatalytic performance.

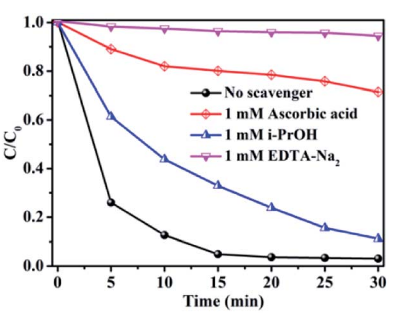

Fig. 15 Photocatalytic activity of $Ag_3PO_4/GO/NiFe_2O_4$ (8%) with different quenchers.

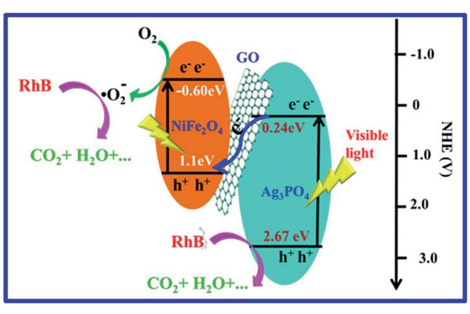

Scheme 1 Schematic diagram of the photocatalytic mechanism of $Ag_3PO_4/GO/NiFe_2O_4$ (8%) with visible-light irradiation.

4. Conclusions

In summary, an effective visible-light-driven $Ag_3PO_4/GO/NiFe_2O_4$ (8%) *Z*-scheme magnetic composite was successfully fabricated by a simple ion-exchange deposition method. Compared to Ag_3PO_4, $NiFe_2O_4$, and $Ag_3PO_4/NiFe_2O_4$, the $Ag_3PO_4/GO/NiFe_2O_4$ (8%) photocatalyst exhibited excellent photocatalytic activity and stability (degradation efficiency was ~96% after 15 min irradiation) for RhB degradation under visible light irradiation. Furthermore, according to the electrochemical and fluorescence measurements, the $Ag_3PO_4/GO/NiFe_2O_4$ (8%) material also showed larger transient photocurrent, lower impedance, and longer fluorescence lifetime (7.82 ns). Comparing the activity result dependence with the characterization results, it was indicated that photocatalytic activity depended on fast charge transfer from Ag_3PO_4 to $NiFe_2O_4$ through GO sheet. h^+ and $\cdot O_2^-$ species played an important role in RhB degradation under visible-light. A possible *Z*-scheme mechanism is proposed for degradation over the $Ag_3PO_4/GO/NiFe_2O_4$ (8%) photocatalyst. This study might provide a promising visible light responsive photocatalyst for the photocatalytic degradation of organic dyes in wastewater.

Conflicts of interest

There are no conflicts to declare.

Acknowledgements

This study was financially supported by the National Natural Science Foundation of China (Grant No. 51768031, No. 51468033) and the Key Research and Development Program in Gansu Province (Grant No. 17YF1NA056).

References

1 C. Mu, Y. Zhang, W. Cui, Y. Liang and Y. Zhu, *Appl. Catal., B*, 2017, **212**, 41–49.
2 M. N. Chong, B. Jin, C. W. K. Chow and C. Saint, *Water Res.*, 2010, **44**, 2997–3027.
3 H. Kyung, J. Lee and W. Choi, *Environ. Sci. Technol.*, 2005, **39**, 2376–2382.
4 Y. Zhao, R. Liu, J. Zhao, L. Xu and C. Sibille, *Bioresour. Technol.*, 2017, **234**, 224–232.
5 B. Bethi, S. H. Sonawane, B. A. Bhanvase and S. P. Gumfekar, *Chem. Eng. Process.*, 2016, **109**, 178–189.
6 X. Y. Huang, X. Y. Mao, H. T. Bu, X. Y. Yu, G. B. Jiang and M. H. Zeng, *Carbohydr. Res.*, 2011, **346**, 1232–1240.
7 L. Du, J. Wu and C. Hu, *Electrochim. Acta*, 2012, **68**, 69–73.

8 C. Bai, X. Xiong, W. Gong, D. Feng, M. Xian, Z. Ge and N. Xu, *Desalination*, 2011, **278**, 84–90.
9 M. F. Hou, L. Liao, W. D. Zhang, X. Y. Tang, H. F. Wan and G. C. Yin, *Chemosphere*, 2011, **83**, 1279–1283.
10 L. Liu, Y. Qi, J. Lu, S. Lin, W. An, Y. Liang and W. Cui, *Appl. Catal., B*, 2016, **183**, 133–141.
11 W. Cui, W. An, L. Liu, J. Hu and Y. Liang, *J. Hazard. Mater.*, 2014, **280**, 417–427.
12 L. Liu, L. Ding, Y. Liu, W. An, S. Lin, Y. Liang and W. Cui, *Appl. Catal., B*, 2017, **201**, 92–104.
13 H. Wang, Y. Liang, L. Liu, J. Hu, P. Wu and W. Cui, *Appl. Catal., B*, 2017, **208**, 22–34.
14 X. Wang, Y. Liang, W. An, J. Hu, Y. Zhu and W. Cui, *Appl. Catal., B*, 2017, **219**, 53–62.
15 S. Fang, K. Lv, Q. Li, H. Ye, D. Du and M. Li, *Appl. Surf. Sci.*, 2015, **358**, 336–342.
16 A. P. Bhirud, S. D. Sathaye, R. P. Waichal, L. K. Nikam and B. B. Kale, *Green Chem.*, 2012, **14**, 2790–2798.
17 Z. Zhang, S. Zhai, M. Wang, H. Ji, L. He, C. Ye, C. Wang, S. Fang and H. Zhang, *J. Alloys Compd.*, 2016, **659**, 101–111.
18 S. K. Apte, S. N. Garaje, G. P. Mane, A. Vinu, S. D. Naik, D. P. Amalnerkar and B. B. Kale, *Small*, 2011, **7**, 957–964.
19 S. Livraghi, M. C. Paganini, E. Giamello, A. Selloni, C. D. Valentin and G. Pacchioni, *J. Am. Chem. Soc.*, 2006, **128**, 15666–15671.
20 Q. Li, B. Guo, J. Yu, J. Ran, B. Zhang, H. Yan and J. R. Gong, *J. Am. Chem. Soc.*, 2011, **133**, 10878–10884.
21 Q. Xiang, J. Yu and M. Jaroniec, *J. Phys. Chem. C*, 2011, **115**, 7355–7363.
22 Y. Bi, S. Ouyang, N. Umezawa, J. Cao and J. Ye, *J. Am. Chem. Soc.*, 2011, **133**, 6490–6492.
23 F. Chen, W. An, L. Liu, Y. Liang and W. Cui, *Appl. Catal., B*, 2017, **217**, 65–80.
24 Y. Bi, H. Hu, S. Ouyang, Z. Jiao, G. Lu and J. Ye, *J. Mater. Chem.*, 2012, **22**, 14847–14850.
25 A. Samal, D. P. Das, K. K. Nanda, B. K. Mishra, J. Das and A. Dash, *Chem. - Asian J.*, 2016, **11**, 584–595.
26 S. S. Patil, M. G. Mali, A. Roy, M. S. Tamboli, V. G. Deonikar, D. R. Patil, M. V. Kulkarni, S. S. Al-Deyab, S. S. Yoon, S. S. Kolekar and B. B. Kale, *J. Energy Chem.*, 2016, **25**, 845–853.
27 S. S. Patil, M. S. Tamboli, V. G. Deonikar, G. G. Umarji, J. D. Ambekar, M. V. Kulkarni, S. S. Kolekar, B. B. Kale and D. R. Patil, *Dalton Trans.*, 2015, **44**, 20426–20434.
28 Y. Li, P. Wang, C. Huang, W. Yao, Q. Wu and Q. Xu, *Appl. Catal., B*, 2017, **205**, 489–497.
29 Q. Wu, P. Wang, F. Niu, C. Huang, Y. Li and W. Yao, *Appl. Surf. Sci.*, 2016, **378**, 552–563.
30 X. Du, J. Wan, J. Jia, C. Pan, X. Hu, J. Fan and E. Liu, *Mater. Des.*, 2017, **119**, 113–123.
31 F. Halouane, Y. Oz, D. Meziane, A. Barras, J. Juraszek, S. K. Singh, S. Kurungot, P. K. Shaw, R. Sanyal, R. Boukherroub, A. Sanyal and S. Szunerits, *J. Colloid Interface Sci.*, 2017, **507**, 360–369.
32 L. Yang, Y. Zhang, X. Liu, X. Jiang, Z. Zhang, T. Zhang and L. Zhang, *Chem. Eng. J.*, 2014, **246**, 88–96.
33 R. M. Khafagy, *J. Alloys Compd.*, 2011, **509**, 9849–9857.
34 W. Fan, M. Li, H. Bai, D. Xu, C. Chen, C. Li, Y. Ge and W. Shi, *Langmuir*, 2016, **32**, 1629–1636.
35 Y. Xia, Z. He, J. Su, B. Tang, K. Hu, Y. Lu, S. Sun and X. Li, *RSC Adv.*, 2018, **8**, 4284–4294.
36 Z. Chen, W. Wang, Z. Zhang and X. Fang, *J. Phys. Chem. C*, 2013, **117**, 19346–19352.
37 A. Iwase, Y. H. Ng, Y. Ishiguro, A. Kudo and R. Amal, *J. Am. Chem. Soc.*, 2011, **133**, 11054–11057.
38 X. j. Chen, Y. Z. Dai, X. Y. Wang, J. Guo, T. H. Liu and F. F. Li, *J. Hazard. Mater.*, 2015, **292**, 9–18.
39 D. Hong, Y. Yamada, T. Nagatomi, Y. Takai and S. Fukuzumi, *J. Am. Chem. Soc.*, 2012, **134**, 19572–19575.
40 Z. Ji, X. Shen, J. Yang, G. Zhu and K. Chen, *Appl. Catal., B*, 2014, **144**, 454–461.
41 F. Wu, X. Wang, M. Li and H. Xu, *Ceram. Int.*, 2016, **42**, 16666–16670.
42 B. K. Kang, M. H. Woo, J. Lee, Y. H. Song, Z. Wang, Y. Guo, Y. Yamauchi, J. H. Kim, B. Lim and D. H. Yoon, *J. Mater. Chem. A*, 2017, **5**, 4320–4324.
43 P. Ma, Y. Yu, J. Xie and Z. Fu, *Adv. Powder Technol.*, 2017, **28**, 2797–2804.
44 T. Zhou, G. Zhang, P. Ma, X. Qiu, H. Zhang, H. Yang and G. Liu, *J. Alloys Compd.*, 2018, **735**, 1277–1290.
45 F. Chen, S. Li, Q. Chen, X. Zheng, S. Fang and Z. Chen, *Mater. Lett.*, 2016, **185**, 561–564.
46 Y. S. Xu and W. D. Zhang, *Dalton Trans.*, 2013, **42**, 1094–1101.
47 Q. Cao, L. Xiao, J. Li, C. Cao, S. Li and J. Wang, *Powder Technol.*, 2016, **292**, 186–194.
48 J. Cao, B. Luo, H. Lin, B. Xu and S. Chen, *J. Hazard. Mater.*, 2012, **217–218**, 107–115.
49 Z. Xing, Z. Ju, J. Yang, H. Xu and Y. Qian, *Nano Res.*, 2012, **5**, 477–485.
50 R. Jin, H. Jiang, Y. Sun, Y. Ma, H. Li and G. Chen, *Chem. Eng. J.*, 2016, **303**, 501–510.
51 C. Liu, D. Yang, J. Yang, Y. Tian, Y. Wang and Z. Jiang, *ACS Appl. Mater. Interfaces*, 2013, **5**, 3824–3832.
52 P. Wang, Y. Li, Z. Liu, J. Chen, Y. Wu, M. Guo and P. Na, *Ceram. Int.*, 2017, **43**, 11588–11595.
53 X. Chen, Y. Dai, J. Guo, T. Liu and X. Wang, *Ind. Eng. Chem. Res.*, 2016, **55**, 568–578.
54 X. Chen, Y. Dai, J. Guo, F. Bu and X. Wang, *Mater. Sci. Semicond. Process.*, 2016, **41**, 335–342.
55 S. S. Patil, M. S. Tamboli, V. G. Deonikar, G. G. Umarji, J. D. Ambekar, M. V. Kulkarni, S. S. Kolekar, B. B. Kale and D. R. Patil, *Dalton Trans.*, 2015, **44**, 20426–20434.
56 S. Hokkanen, E. Repo, L. J. Westholm, S. Lou, T. Sainio and M. Sillanpää, *Chem. Eng. J.*, 2014, **252**, 64–74.
57 J. Ma, J. Zou, L. Li, C. Yao, T. Zhang and D. Li, *Appl. Catal., B*, 2013, **134–135**, 1–6.
58 S. Krungchanuchat, N. Ekthammathat, A. Phuruangrat, S. Thongtem and T. Thongtem, *Mater. Lett.*, 2017, **201**, 58–61.
59 M. Srivastava, S. Chaubey and A. K. Ojha, *Mater. Chem. Phys.*, 2009, **118**, 174–180.
60 G. Dixit, *Adv. Mater. Lett.*, 2012, **3**, 21–28.

61 B. Senthilkumar, R. Kalai Selvan, P. Vinothbabu, I. Perelshtein and A. Gedanken, *Mater. Chem. Phys.*, 2011, **130**, 285–292.
62 Y. Tong, T. Lu, S. Xu and L. Xu, *Mater. Lett.*, 2017, **200**, 79–82.
63 K. Wang, J. Xu, X. Hua, N. Li, M. Chen, F. Teng, Y. Zhu and W. Yao, *J. Mol. Catal. A: Chem.*, 2014, **393**, 302–308.
64 P. Tan, X. Chen, L. Wu, Y. Y. Shang, W. Liu, J. Pan and X. Xiong, *Appl. Catal., B*, 2017, **202**, 326–334.
65 C. Cui, Y. Wang, D. Liang, W. Cui, H. Hu, B. Lu, S. Xu, X. Li, C. Wang and Y. Yang, *Appl. Catal., B*, 2014, **158–159**, 150–160.
66 W. Yao, B. Zhang, C. Huang, C. Ma, X. Song and Q. Xu, *J. Mater. Chem.*, 2012, **22**, 4050–4055.
67 B. Lu, N. Ma, Y. Wang, Y. Qiu, H. Hu, J. Zhao, D. Liang, S. Xu, X. Li, Z. Zhu and C. Cui, *J. Alloys Compd.*, 2015, **630**, 163–171.
68 D. Jiang, J. Zhu, M. Chen and J. Xie, *J. Colloid Interface Sci.*, 2014, **417**, 115–120.
69 N. Wang, Y. Zhou, C. Chen, L. Cheng and H. Ding, *Catal. Commun.*, 2016, **73**, 74–79.
70 L. Shi, F. Wang, L. Liang, K. Chen, M. Liu, R. Zhu and J. Sun, *Catal. Commun.*, 2017, **89**, 129–132.
71 N. Shao, J. Wang, D. Wang and P. Corvini, *Appl. Catal., B.*, 2017, **203**, 964–978.
72 J. Xian, D. Li, J. Chen, X. Li, M. He, Y. Shao, L. Yu and J. Fang, *ACS Appl. Mater. Interfaces*, 2014, **6**, 13157–13166.
73 S. Soedergren, A. Hagfeldt, J. Olsson and S. E. Lindquist, *J. Phys. Chem.*, 1994, **98**, 5552–5556.
74 D. Wang, D. Choi, J. Li, Z. Yang, Z. Nie, R. Kou, D. Hu, C. Wang, L. V. Saraf, J. Zhang, I. A. Aksay and J. Liu, *ACS Nano*, 2009, **3**, 907–914.
75 T. Lu, Y. Zhang, H. Li, L. Pan, Y. Li and Z. Sun, *Electrochim. Acta*, 2010, **55**, 4170–4173.
76 H. L. Guo, X. F. Wang, Q. Y. Qian, F. B. Wang and X. H. Xia, *ACS Nano*, 2009, **3**, 2653–2659.
77 Y. Zhang, W. Cui, W. An, L. Liu, Y. Liang and Y. Zhu, *Appl. Catal., B*, 2018, **221**, 36–46.
78 H. Wang, Y. Liang, L. Liu, J. Hu and W. Cui, *J. Hazard. Mater.*, 2018, **344**, 369–380.
79 Y. Liang, S. Lin, L. Liu, J. Hu and W. Cui, *Appl. Catal., B*, 2015, **164**, 192–203.
80 Q. Liu, J. Huan, N. Hao, J. Qian, H. Mao and K. Wang, *ACS Appl. Mater. Interfaces*, 2017, **9**, 18369–18376.
81 D. Wang, F. Jia, H. Wang, F. Chen, Y. Fang, W. Dong, G. Zeng, X. Li, Q. Yang and X. Yuan, *J. Colloid Interface Sci.*, 2018, **519**, 273–284.
82 Y. Hong, Y. Jiang, C. Li, W. Fan, X. Yan, M. Yan and W. Shi, *Appl. Catal., B*, 2016, **180**, 663–673.
83 H. Katsumata, T. Sakai, T. Suzuki and S. Kaneco, *Ind. Eng. Chem. Res.*, 2014, **53**, 8018–8025.
84 M. Ge, Y. Chen, M. Liu and M. Li, *J. Environ. Chem. Eng.*, 2015, **3**, 2809–2815.

